COMPUTATIONAL INVESTIGATION OF DIESEL NOZZLE INTERNAL FLOW DURING THE COMPLETE INJECTION EVENT

Salvador, F.J. (*), De la Morena, J., Bracho, G., Jaramillo, D.

CMT-Motores Térmicos. Universitat Politècnica de València, Spain

(*) Corresponding author:

Dr. F. Javier Salvador, fsalvado@mot.upv.es

CMT-Motores Térmicos, Universitat Politècnica de València

Camino de Vera s/n, E-46022 Spain.

Telephone: +34-963879658

FAX: +34-963877659

ABSTRACT

Currently, diesel engines are calibrated using more and more complex multiple injection strategies. Under these conditions, the characteristics of the flow exiting the fuel injector are strongly affected by the transient interaction between the needle, the sac volume and the orifices, which are not yet clear. In the current paper, a methodology combining a 1D injector model and 3D-CFD simulations is proposed. First, the characteristics of the nozzle flow have been experimentally assessed in transient conditions by means of injection rate and momentum flux measurements. Later, the 3D-CFD modeling approach has been validated at steady-state fixed lift conditions. Finally, a previously developed 1D injector model has been used to extract the needle lift profiles and transient pressure boundary conditions used for the full-transient 3D-CFD simulations,

using Adaptative Mesh Refinement (AMR) strategies to be able to simulate the complete injection rate starting from 1 micrometer lift.

KEYWORDS: nozzle, modelling, Diesel, dynamic, moving-mesh

NOMENCLATURE

A	Constant for discharge coefficient vs. Reynolds equation
A_{eff}	Effective area
A_o	Geometrical area
C_a	Area coefficient
C_c	Contraction coefficient
C_d	Discharge coefficient
$C_{d,max}$	Maximum value of discharge coefficient vs. Reynolds
C_v	Velocity coefficient
D_o	Geometrical nozzle diameter
$\dot{m}$	Mass flow
$\dot{M}$	Momentum flux
P_{back}	Discharge pressure
P_{inj}	Injection pressure
u_o	Outlet nozzle orifice velocity
u_{th}	Theoretical outlet orifice velocity, $u_o = \sqrt{\frac{2 \cdot (P_{inj} - P_{back})}{\rho_f}}$

Greek Symbols

ΔP	Pressure drop, $\Delta P = P_{inj} - P_{back}$
ρ_f	Fuel density
υ_f	Kinematic viscosity
λ	Flow coefficient or theoretical Reynolds number

1. INTRODUCTION.

The design of modern Diesel engines is focused on the reduction of pollutant emissions as well as fuel consumption due to the strict emission standards and global environmental awareness [1, 2] . Both aspects are related to the fuel-air mixing and combustion processes. In particular, several studies have observed how the formation of soot particles, which are one of the most critical pollutants in diesel engines, is directly related to the equivalence ratio at the lift-off length, which is an indicator of the fuel-air mixing efficiency [3–5]. Furthermore, brake thermal efficiency and combustion efficiency are also strongly impacted by the spray characteristics [6, 7].

Fuel-air mixing and spray formation depend on the fuel injector design. R. Payri et al. [8] showed that the injector technology affects spray formation and combustion performance, with piezoelectric actuated injectors being characterized by shorter evaporation time and ignition delay. Similar results were obtained by Park et al. [9], linking also the use of piezoelectric injectors to a more efficient spray atomization. Most of these effects are linked to the different dynamic behavior of these injector technologies, which affect the transient evolution of the needle lift, known to impact the internal flow and near-nozzle spray features in both diesel and gasoline direct injection systems [10–12]. Additionally, the internal geometry of the nozzle, and in particular of the discharge holes, is also critical in spray formation [13–15].

As a consequence of their relevance into the engine development process, different modeling approaches have been investigated over the years to predict the different physical phenomena related to fuel injection. Payri et al. [16] have used 1D-modeling tools to simulate the transient needle lift and mass flow rate of injectors, allowing to evaluate the effects of different fuel temperatures. Similar tools have been used by other authors to predict the effect of the injector technology on the instantaneous mass flow rate [17, 18]. Desantes et al. [19] evaluated a 1D-model based on momentum flux data to assess local velocity and mass fraction distribution inside the spray. Different authors have also analyzed the influence of the nozzle geometry on the internal flow, and in particular the eventual cavitation formation, through experimental and computational tools [20–24]. Internal nozzle flow simulations can also be coupled with spray models to have the complete picture of all the related phenomena [25].

To approach coupled internal flow and spray simulations in realistic engine conditions, it is necessary first to develop internal flow models working at transient needle lift conditions. This implies the usage of moving mesh techniques. Traditionally, these strategies are based on stretching a set of pre-defined cells [26, 27]. For diesel injector applications, if the mesh is configured to provide meaningful resolution at high needle lifts, then very narrow cells with high skewness factors appear when the needle is close to its seat, inducing numerical instabilities and affecting the model predictability. This has limited the minimum needle lift for transient simulations to a value between 10 and 20 μm [28, 29]. Nevertheless, the nozzle internal flow behaves in a significantly different way at very low needle positions due to the different flow direction induced [13, 30], which influences end-of-injection related phenomena like fuel dribble, linked to higher smoke and hydrocarbon emissions [7]. Battistoni et al. [31] performed a coupled internal flow and spray simulation with moving mesh for a single-hole nozzle. In their work, the minimum lift was set to 2.5 μm for the injection rate opening and 10 μm for the needle closure, after which, a transition strategy to a fully close needle simulation was developed. These two stages of the injection event were characterized in two different simulations, in order to maintain a reasonable computational time. Such methodology allowed the study of the spray dynamics in a more realistic way, even though some of the internal flow characteristics at very low needle lifts could not be captured.

In the current paper, an Adaptive Mesh Refinement (AMR) methodology implemented in CONVERGE [32] has been evaluated for internal nozzle flow modeling of a diesel injector. The strategy has been applied to both fixed and moving needle conditions. At fixed lifts, this methodology has the potential to reduce computational time by automatically refining the mesh only in the areas of the domain where needed according to velocity gradients. When computing a transient injection event with moving needle conditions, AMR has the advantage of being able to create new layers of cells as the needle moves up, which improves the modeling capability and stability at very low lifts (1 μm for the current paper).

The paper is divided in 6 sections. Section 2 presents the experimental tools used to characterize the hydraulic behavior of the injector used in this research. The results of this characterization, used to validate the CFD model, are summarized in Section 3. The outcomes of the modeling approach are detailed in two sections: one for the steady state lift simulations (4), and a second one that analyzes the transient injection event (5). Finally, the main conclusions of the study are drawn in Section 6.

2. EXPERIMENTAL TOOLS.

2.1 Injection system, nozzle description and fluid properties.

In this research, a common-rail fuel injection system able to reach up to 180 MPa is used. This system includes a solenoid-driven Bosch injector mounting a seven-orifices microsac nozzle. To perform the numerical investigations summarized in sections 4 and 5, the nozzle geometry has been obtained using a silicone mold technique explained in [33]. This technique is based on the imaging of the molds using an electron microscope (Figure 1.a). The mold is analyzed with different levels of resolution to detect the geometrical features of the nozzle sac and orifices (Figure 1.b). The post-processing of the orifices allows to determine all the critical parameters, such as the rounding radii or the inlet and outlet diameters, with an accuracy of ±2 μm (Figure 1.c and 1.d). The orifice length has been directly set to 1 mm according to the nozzle nominal dimensions provided by the fuel injector manufacturer.

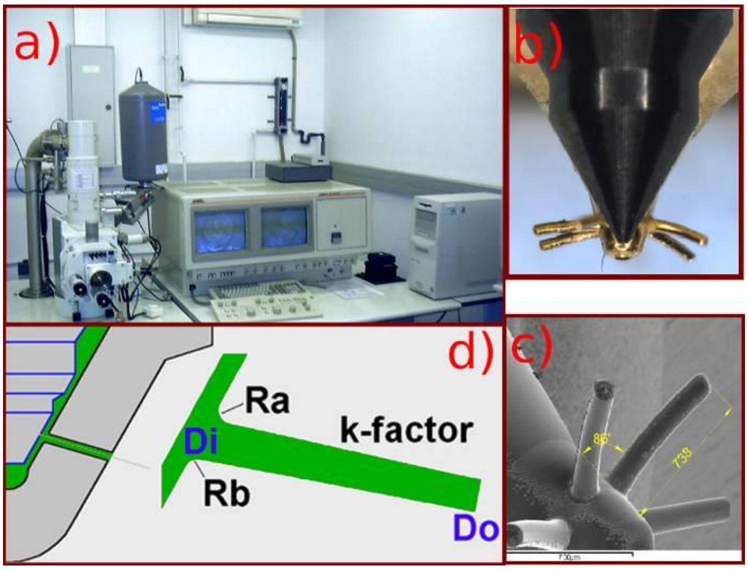

Fig. 1. Nozzle geometry determination by the silicone molding technique.

The specific values of these parameters for the nozzle of study are given in Table 1. The nozzle conicity degree is evaluated by means of the *k-factor*, which is defined as:

$$k - factor = \frac{D_i - D_o}{10} \tag{1}$$

Table 1. Geometrical parameters of the nozzle.

R_a [μm]	R_b [μm]	R [μm]	D_i [μm]	D_m [μm]	D_o [μm]	k-factor	Length [μm]
29±8	22±6	25.5±7	143±2.3	130±1.4	124±2.2	1.9±0.2	715±15

As can be seen from the table, *k-factor* is 1.9, meaning that the nozzle orifices have a relatively high degree of convergence. Thus, according to previous experiences in the literature, low (or null) cavitation is *a priori* expected [34, 35].

The value of *R* in Table 1, is the rounding radius at the inlet orifice, which together the *k-factor* are the most important factors having influence on cavitation phenomena [36, 37]. It can be determined either for the upper part of the orifice inlet, R_a, or for the bottom part of the orifice inlet, R_b. Again, the values obtained indicate the low probability for cavitation formation inside the nozzle orifices.

As far as the fluid used for the experiments is concerned, it was a Repsol Diesel CEC RF-06-99 fuel. Its most important physical properties were characterized in a previous work [38]. In particular, the correlations available for the fuel density and viscosity as a function of pressure and temperature are:

$$\begin{aligned} \rho_f &= 830.6 - 1.021(T-298) + 1.53\cdot10^{-3}(T-298)^2 + 0.566(P-0.1) \\ &- 6.4\cdot10^{-4}(P-0.1)^2 + 0.013(P-0.1)(T-298) \end{aligned} \tag{2}$$

$$\mu_f = \mu_0 \cdot 10^{\left[\left(-1.48+5.86\mu_0^{0.181}\right)\left(\frac{P-0.1013}{1000}\right)\right]} \tag{3}$$

$$\mu_0 = 3.4571 \cdot \exp\left[-0.0283(T-298)\right] \tag{4}$$

Where ρ_f is the fuel density in kg/m^3, μ_f is the fuel dynamic viscosity in mPa·s, μ_0 is the fuel dynamic viscosity at 0.1 MPa of pressure (also in mPa·s), P is the fuel pressure in MPa and T is the fuel temperature in K.

2.2 Injection rate meter and spray momentum test rig.

A wide experimental hydraulic characterization was made based on mass flow rate and momentum flux measurements. The first were carried out by means of an Injection Rate Discharge Curve Indicator system based on Bosch method [39]. The measuring principle consists in measuring the pressure increase when injecting into a fuel-filled tube. This pressure increase is related to the injected mass flow rate through the fuel sound speed, among others factors. The registered signals should be processed in order to filter a cumulative phenomenon deemed to be important especially for long injections, following the procedure described in [40]. The uncertainty in the actual injection rate when using the previously described methodology has been estimated in ±1.5%.

As far as the momentum flux test rig is concerned, with this device it is possible to measure the spray momentum flux by capturing the impact force of the spray on a surface. The force is transmitted to a piezo-electric pressure sensor previously calibrated with an accelerometer. The uncertainty of this measurement is approximately ±1.8%. Details of the measuring principle and a picture of this test rig are given in [41]. This kind of measurement, combined with the mass flow rate results, can be used as a tool to assess the orifice-to-orifice dispersion in a nozzle, and also for determining the effective injection velocity and other non-dimensional flow parameters, which help describing the characteristics of the inner nozzle flow.

2.3 Test matrix.

In order to have a complete hydraulic characterization at different injection conditions, i.e., different values of the Reynolds number, a wide test matrix has been used. Table 2 reports the operating conditions in terms of injection pressures and backpressures (discharge pressure). Each of them has been tested for three energizing times of 1ms, 1.5 ms and 2 ms. All the possible combinations lead to a total of 108 points.

Table 2. Test matrix for the mass flow rate and momentum flux measurements.

Injection Pressure [MPa]	**Back Pressures [MPa]**
30-80-130-180	0.5 – 1 – 3 – 5 – 7 – 9 – 11 – 13 - 15

3. HYDRAULIC CHARACTERIZATION RESULTS.

In this section, the results of the hydraulic characterization are reported and analyzed.

3.1 Mass flow rate results.

In Figure 2, the mass flow rate results for P_{inj}=30 MPa and P_{back}= 3 MPa are plotted for three different values of Energizing Time (1 ms, 1.5 ms and 2 ms). As expected, the mass flow rates are identical at the beginning of the injection during the needle opening, and they show the same steady mass flow rate. The small perturbation observed in the different registered signals is related to the electrovalve closing. As can be seen in the upper part of the figure, where the intensity of the energizing electrical current is plotted, this perturbation coincides with the instant at which the current intensity ceases. The pressure in the line feeding the injector is also represented in the middle part of Figure 2, and, again, the differences between them are due to the different energizing time of each injection.

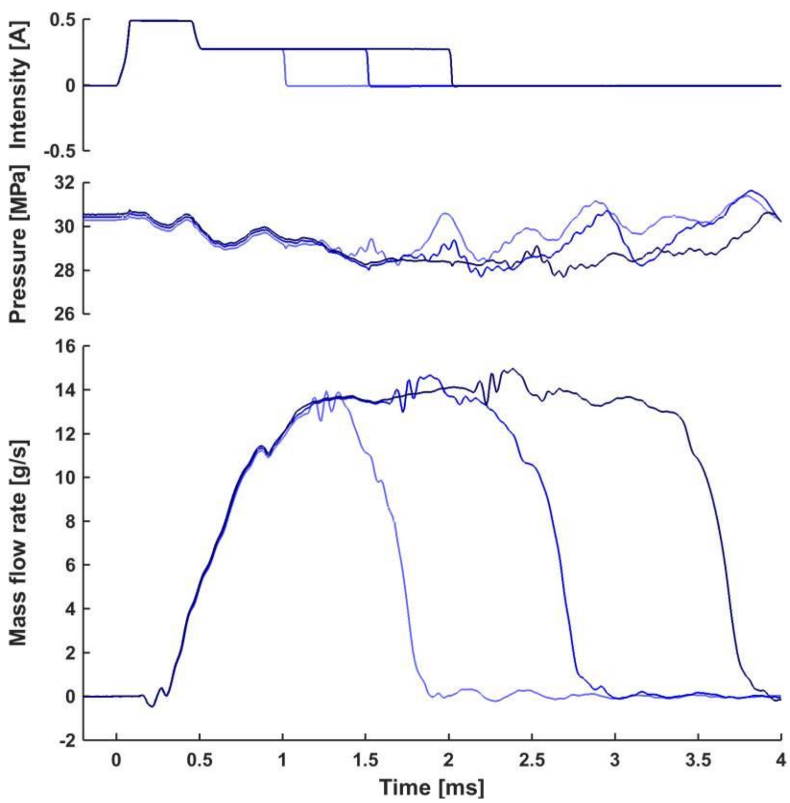

Fig. 2 Mass flow rate for P_{inj}= 30 MPa, P_{back}= 3 MPa and different Energizing Times.

In Figure 3, the mass flow rates measurements for the injection pressure of 30 MPa and nine different backpressures are displayed. The points correspond to the energizing time of 2 ms. The main differences between the curves are related to the maximum mass flow value and the end of injection time. According to equation (5), the mass flow at steady-state conditions is directly proportional to the square root of the pressure drop along the injector:

$$\dot{m} = \rho_f \cdot A_{eff} \cdot u_{eff} = \rho_f \cdot C_a \cdot A_o \cdot C_v \cdot u_{th} = C_d \cdot A_o \cdot \sqrt{2\Delta P \cdot \rho_f} \quad (5)$$

Being ΔP the pressure drop defined as $\Delta P = P_{inj} - P_{back}$; A_o and A_{eff} the geometrical and effective outlet sections of the nozzle orifices, respectively; u_{th} the theoretical outlet velocity according to Bernoulli's equation and C_d, C_v and C_a are the discharge, velocity and area coefficients, defined as:

$$C_d = \frac{\dot{m}}{\dot{m}_{th}} = \frac{\dot{m}}{\rho_f \cdot A_o \cdot u_{th}} \quad (6)$$

$$C_v = \frac{u_{eff}}{u_{th}} = \frac{u_{eff}}{\sqrt{2\Delta P / \rho_f}} \quad (7)$$

$$C_a = \frac{A_{eff}}{A_o} = \frac{C_d}{C_v} \quad (8)$$

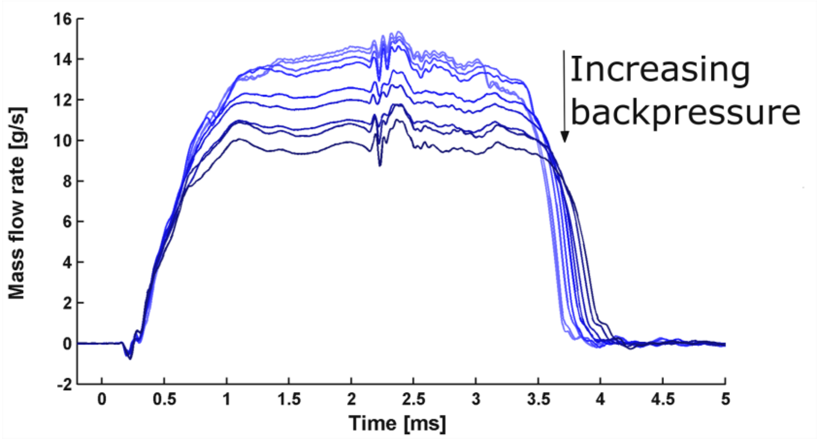

Fig. 3. Mass flow rates for P_{inj}= 30 MPa and different backpressures (0.5-15 MPa).

Apart from the effect seen on the maximum mass flow, increasing the backpressure also leads to slower needle dynamics, which results in a longer delay from the end of the electrical signal to the hydraulic closing of the injector. This is mainly due to the stronger force that opposes to the needle motion when the backpressure is higher. At the start of the injection event, the control volume is at pressure levels close to the injection pressure, and the contribution of the control pressure to the needle dynamics is small.

When the electrovalve stops being energized and the needle starts closing, both the control volume and the needle are at similar pressure values, and the weight of the backpressure force is more significant, resulting in the longer injection duration for higher backpressure previously mentioned.

Figure 4 shows the same kind of results for P_{inj} = 180 MPa. In this case, being the injection pressure much higher, the weight of the backpressure variation on the pressure drop value is small, and consequently the injection rate curves are very close one to another. Additionally, the effect of the backpressure on the needle dynamics, and consequently on the opening and closing slopes of the injection rate, are minimal.

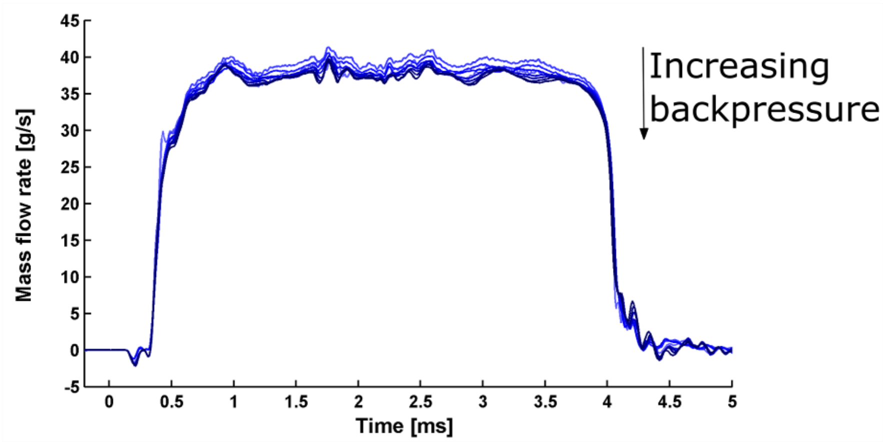

Fig. 4. Mas flow rates for P_{inj}= 180 MPa and different backpressures (0.5-15 MPa).

3.2 Momentum flux results.

Figure 5 summarizes the momentum flux results obtained for P_{back}= 5 MPa conditions. The left hand side of the figure represents the momentum flux from four of the seven discharge orifices of the nozzle for P_{inj}= 130 MPa, showing that there is small hole-to-hole dispersion in the injector of study, which will allow performing the numerical simulations for just one of the nozzle orifices. The right hand side of the figure shows the evolution of the momentum flux as a function of the injection pressure.

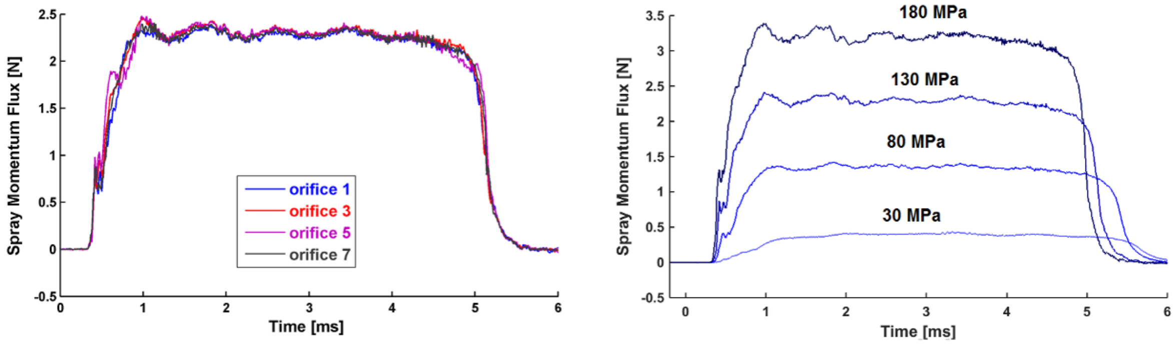

Fig. 5. Left: momemtum flux for P_{inj}= 130 MPa, P_{back}= 5 MPa for different orifices. Right: momentum flux for P_{back}= 5 MPa and different injection pressures

The main difference among them relates to their maximum value (at steady-state conditions), which can be evaluated assuming steady-state conditions according to equation (9):

$$\dot{M} = \dot{m} \cdot u_{eff} = \rho_f \cdot A_{eff} \cdot u_{eff}^{2} = \rho_f \cdot C_a \cdot A_o \cdot C_v^{2} \cdot u_{th}^{2} = C_M \cdot A_o \cdot 2\Delta P \qquad (9)$$

Thus, the stationary momentum flux grows linearly with the pressure drop along the injector, which is consistent with the results previously observed. Regarding the dynamic behavior of this parameter, it is evident again that higher values of ΔP lead to faster injection dynamics and shorter hydraulic durations for the same energizing time, as it was already observed when analyzing the injection rate data.

3.3 Flow coefficients behavior.

From the analysis introduced in equation (9), it can be immediately seen that the effective outlet velocity of the flow can be obtained from the combination of the stationary mass flow and momentum flux results:

$$u_{eff} = \frac{\dot{M}}{\dot{m}} \qquad (10)$$

Figure 6 depicts the steady-state conditions values of mass flow, momentum flux and effective velocity obtained from the previous measurements. Stationary mass flow grows linearly with the square root of the pressure drop, consistently with the analysis performed in equation (5) and the fact that no cavitation occurs inside the nozzle orifices, as it was expected from their geometry. Similar result is obtained in terms of the spray momentum, but considering in this case the pressure drop, consistently with equation (9). Being the effective velocity the ratio among the two, its evolution is also linear with the square root of *ΔP*, with values ranging approximately 200-600 m/s.

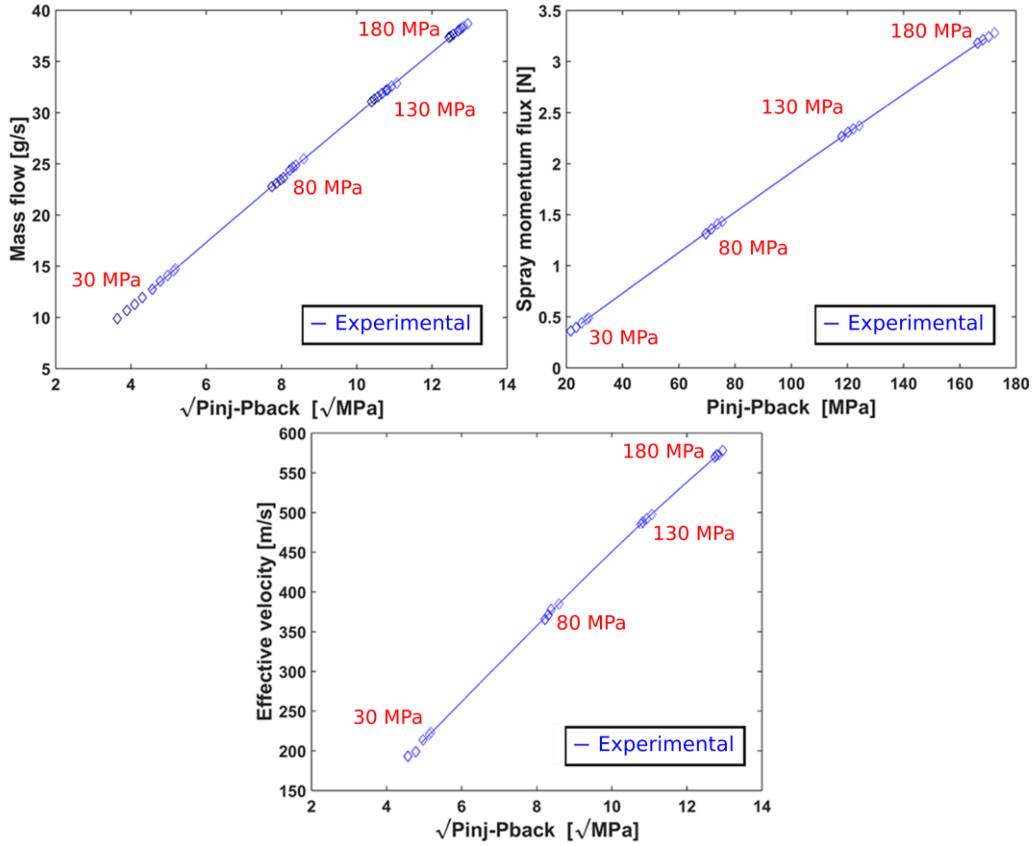

Fig. 6. Steady mass flow rate, spray momentum and effective velocity.

Apart from the effective velocity, it is also possible to determine the main flow coefficients (i.e., the discharge coefficient -C_d- and the velocity coefficient C_v-) from the combined analysis of mass flow and momentum flux, using equations (6) and (7). The values finally reached are depicted in Figure 7.

The discharge coefficient shows an asymptotic increase behavior with the square root of the pressure drop, with a maximum value of approximately 0.87. This is due to the different turbulent characteristics of the flow. At low values of ΔP (i.e., low values of outlet velocity), the characteristic Reynolds number at the outlet of the nozzle is low, and consequently the turbulence intensity is moderate, characteristic of a laminar/transitional regime. At these conditions, the discharge coefficient tends to grow with the Reynolds number according to the expression [42]:

$$C_d = C_{d,\max} - \frac{A}{\sqrt{\mathrm{Re}}} \tag{11}$$

With $C_{d,max}$ and A being coefficients depending on the geometrical and hydraulic characteristics of the nozzle. For the conditions along the study, the Reynolds number defined from the geometrical and the velocity calculated from Bernoulli's equation ranges approximately 10900-37700.

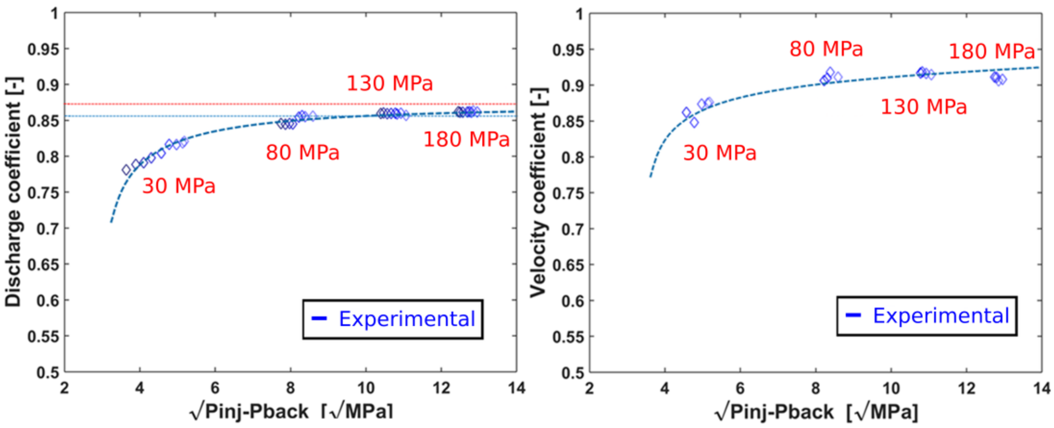

Fig. 7. Non-dimensional flow parameters: C_d and C_v.

As the pressure drop increases, the outlet Reynolds number also grows, and the turbulent regime is already developed; therefore, the discharge coefficient becomes almost independent from the Reynolds number. In the case of the velocity coefficient, the behavior is analogous to the one already described for the discharge coefficient, since the nozzle shows no cavitation and the area coefficient is almost constant.

4. NOZZLE SIMULATION IN STEADY-STATE (MAXIMUM LIFT).

In the current section, the simulation work at fixed needle lift conditions will be discussed. First, the characteristics of the mesh used for such study and the main simulation settings are described. Later on, the conditions at the nozzle orifice outlet obtained through these computations are validated against the flow coefficients obtained from the hydraulic characterization results.

4.1 Mesh construction and simulations setup.

For the computational study a sector geometry of 51.4º of the nozzle, representing one of the seven orifices of the nozzle, will be considered. This approach can be considered acceptable taking into account the low hole-to-hole dispersion already observed during the momentum flux measurements. As stated during the introduction, an Adaptive Mesh Refinement technique, for which the mesh is automatically refined in the areas needed according to the information from the velocity fields at every time step, has been selected in CONVERGE. Such strategy allows reducing the total amount of cells compared to a static mesh approach, saving CPU time for the simulations.

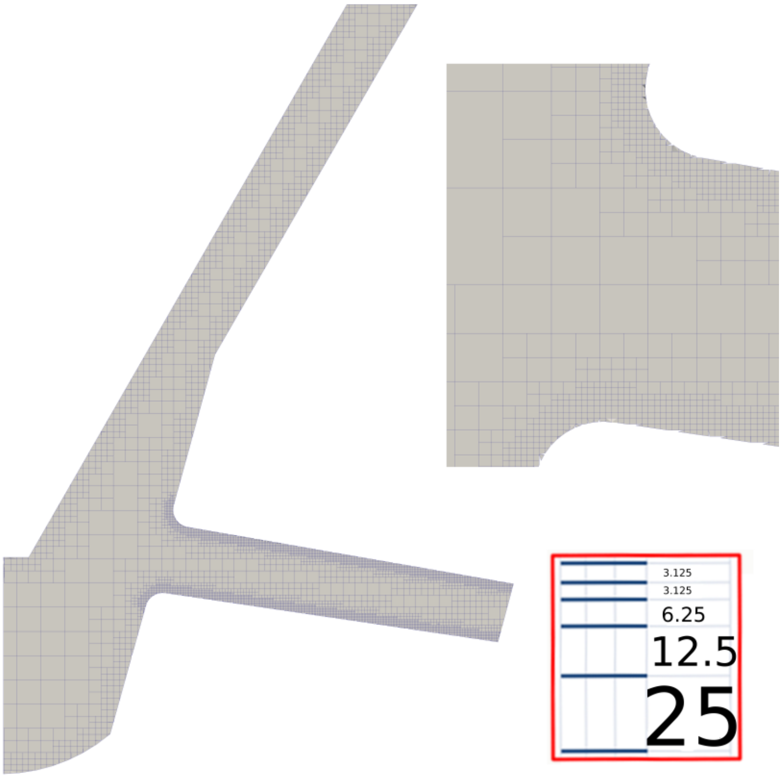

Fig. 8. Geometry and sample mesh for the simulation (cell size in μm)

Figure 8 shows the detail of the geometry and an image of the final mesh used for the study at the initial time step. The inlet and outlet boundary conditions in the domain have been set as constant pressure, and equal to the values of injection and discharge pressure used during the experimental activities. It ought to be considered that these pressures are not measured exactly in the location of the boundary conditions, which induces some uncertainties for the validation process. Nevertheless, in the case of the injection pressure, previous experiences show that the pressure losses from the rail up to the needle seat are low compared to those occurring in the needle seat itself [43]. For the nozzle and needle walls, a non-slip boundary condition (i.e. the fluid velocity is the same as the velocity of the solid boundary) has been set. About turbulence, Re-Normalization Group (RNG) k-epsilon model has been chosen over the standard k-epsilon because the modelization of the effective viscosity makes possible a better handling of low Reynolds numbers and near-wall flows according to previous experiences from diesel internal nozzle flow simulations [44]. For the fluid properties, the values of density and viscosity have been computed using equations (2-4), particularized for the outlet pressure and a temperature level of 40ºC. All simulations assume incompressible and isothermal conditions, which means that the fluid properties are constant along the complete computational domain.

During the initial stages of the investigation, preliminary simulations have been carried out to select the most appropriate combination of numerical schemes for the discretization of the Navier-Stokes equations and the mesh size parameters. In terms of the numerical schemes, both first order (upwind) and second order (central) approaches have been explored. In any case, PISO algorithm combined with Successive Over-Relaxation (SOR) method has been used for solving the transport equations.

Regarding the mesh sizing, in the AMR methodology available in CONVERGE, it is based on two parameters: the base cell size (dx_{base}), representing the maximum size in the domain, and the embed-scale parameter (*emb*), which is related to the minimum size of the cells close to the walls (dx_{min}), according to the following expression:

$$dx_{\min} = \frac{dx_{base}}{2^{emb}} \tag{12}$$

For the current case, 3 levels for the base cell size (40, 50 and 60 µm) and three levels for the embed-scale parameter inside the nozzle orifice (2, 3 and 4) have been explored on a single case (P_{inj} = 80 MPa, P_{back} = 7 MPa) to explore the effects of these parameters on the model accuracy. Additionally, different number of layers at the initial cell size have been considered, starting at a minimum value of 2.

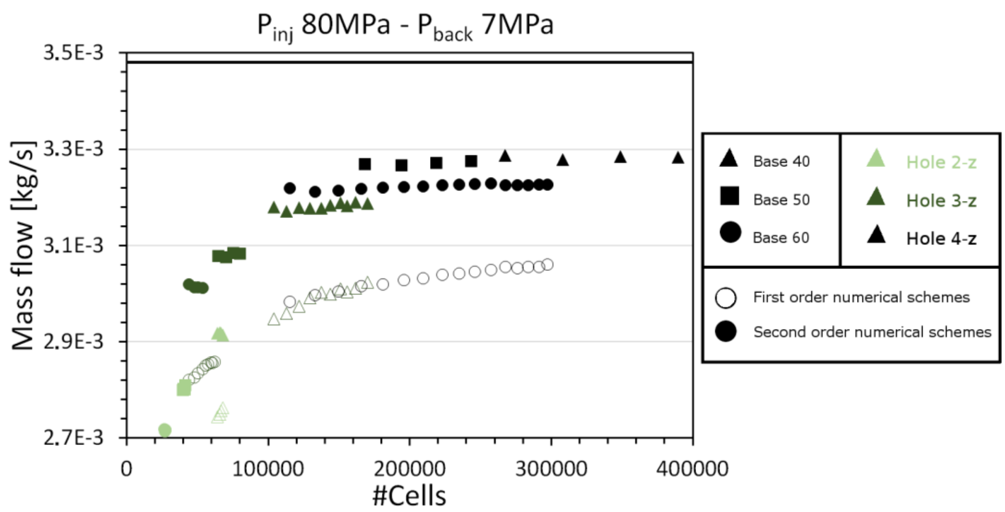

Fig. 9. Mesh sensitivity study.

In Figure 9, the solid black line represents the experimental value of mass flow through the nozzle orifice at these operating conditions; void symbols are used for the first order numerical schemes, while solid symbols indicate that second order schemes are selected (in both cases, upwind schemes are used); the kind of symbol is linked to the base cell size value and, finally, the color is related to the value of the embed-scale parameter inside the orifice. For each combination of numerical scheme, base size and embed-scale parameter, different configurations with different number of layers at the minimum cell size, starting at a value of 2, have been screened. As the number of layers gets higher, the total number of cells increases significantly. For example, in the case of the Base 60, second order schemes, embed-scale parameter 4, the total number of cells in the computational domain increase from ~115000 to ~300000 when changing the number of layers from 2 to 16.

Looking at the results, the first conclusion that can be drawn is that the first order scheme shows very significant sensitivity to number of layers, while the second order scheme is almost insensitive to this variable. For this reason, the number of layers will be set to 2 in order to reduce the computational effort. For the cell parameters, it can be observed how the combination of a base size of 40 µm and an embed-scale value of 4 is providing the closer results to the experimental results, with an accuracy of approximately 5% in terms of the mass flow. Nevertheless, it can be seen that the values are very close to those achieved for the 50 µm and an embed-scale value of 4 (only 0.3% accuracy improvement), while the total number of cells (and consequently the computational effort) can be significantly reduced. Thus, these values will be used for the rest of the study. Other settings of the model are reported in Table 3.

Table 3. Tolerances and relaxation factors for the main physical parameters in CFD.

Parameter	**Tolerance**	**Relaxation Factor**
Velocity	10^{-6}	0.5
Pressure	10^{-8}	1
Density	10^{-6}	0.5
Turbulent kinetic energy	10^{-3}	0.5
Turbulent dissipation	10^{-3}	0.5

Figure 10 shows the maximum, mean and minimum y^+ values calculated in the cells inside the nozzle orifice, where the higher flow velocities and turbulent levels are reached. As it can be seen the values achieved are rather low, with a mean value lower than 0.5. This is consistent with the very low minimum cell size used along the simulations (3.125 µm), and can be seen as another indicator of the consistency of the mesh characteristics previously chosen during the mesh sensitivity study. Thanks to the high level of refinement used, no particular wall functions were necessary for these simulations.

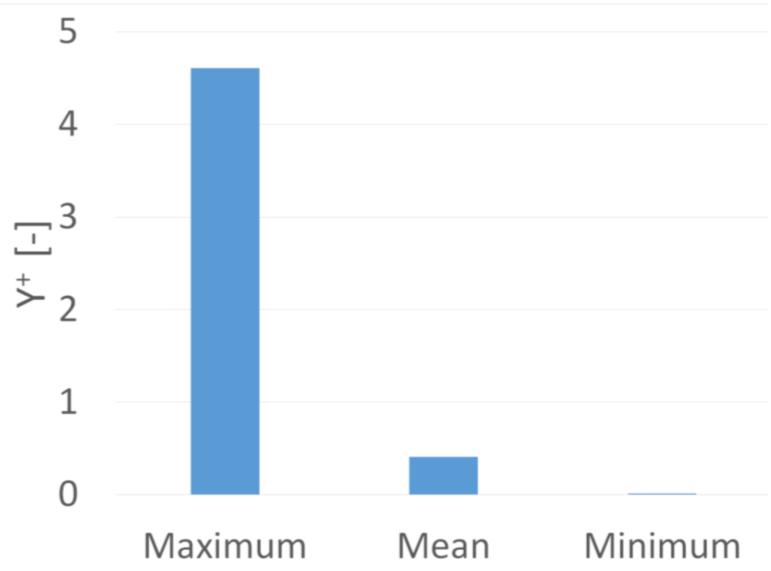

Fig. 10. Computed y^+ values inside the orifice

4.2 Validation of results in steady-state conditions.

Figure 11 shows the results of the validation of the stationary AMR simulations at maximum needle lift. In particular, the left hand side of the figure shows the comparison of experimental vs. computations for the stationary mass flow rate, while on the right hand side the effective velocity values are depicted. As it can be observed, the results of the simulation are almost overlapped with the experiments at low injection pressure level (30 MPa, $\Delta P^{1/2} \approx 5500\ Pa$), while the simulations tend to deviate from the experimental results as the injection pressure gets high, with a maximum of 10% at 180 MPa ($\Delta P^{1/2} \approx 13000\ Pa$). It has to be noted that, while the fluid properties have been considered constant, in reality both density and viscosity tend to increase together with the fuel pressure. Since density and viscosity have been computed at the backpressure conditions, there is an underestimation of these properties, especially in the areas corresponding to the needle seat, the sac and the inlet section of the orifice. While higher viscosities would tend to reduce the nozzle permeability thanks to the increase of the viscous friction losses, the effect of density and viscosity on the local Reynolds number and the turbulence characteristics could partially explain the behavior of the simulation results. Another potential cause of the differences between experiments and simulations is related to the uncertainties in the nozzle geometry determination, which are related to the standard deviation values provided in Table 1. This subject will be analyzed in more details in the next section for the transient simulations results.

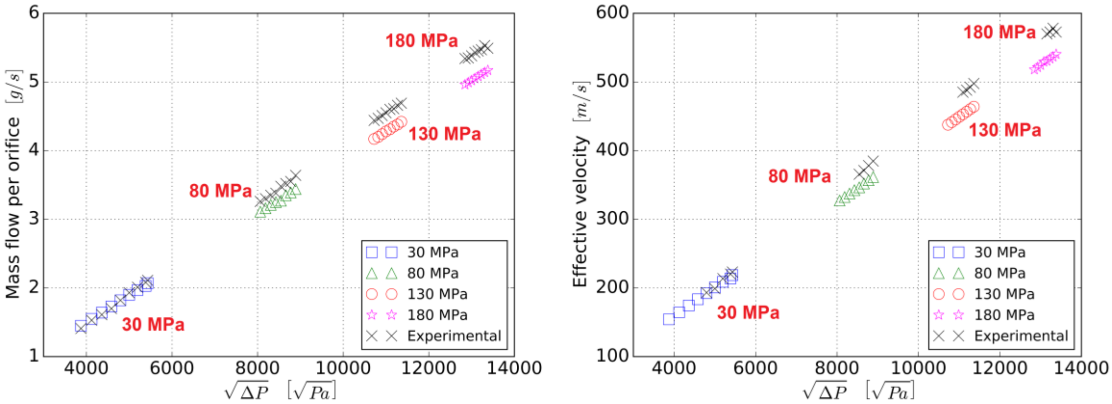

Fig. 11. Numerical results validation for mass flow rate and effective velocity.

5. NOZZLE SIMULATION IN TRANSIENT CONDITIONS.

In the next lines, the procedure used to perform the moving needle lift simulations and the consequent injection rate results are analyzed.

5.1 Needle lift law derivation from 1D Modelling.

One of the most critical aspects of performing transient internal nozzle flow simulations is how to impose the needle lift law itself, since this information is generally not available experimentally. The proposal used in this study has been to obtain the needle lift profiles from a 1D model of the injector, previously developed in Amesim [45], which is a multidisciplinary 1D-model platform based on Bond Graph technique. The needle lift profiles obtained through the 1D model are then imposed as boundary conditions for the 3D moving-mesh model. It has to be noted that the 3D simulations do not start at a completely closed needle condition. Indeed a minimum needle lift of 1 μm has been set

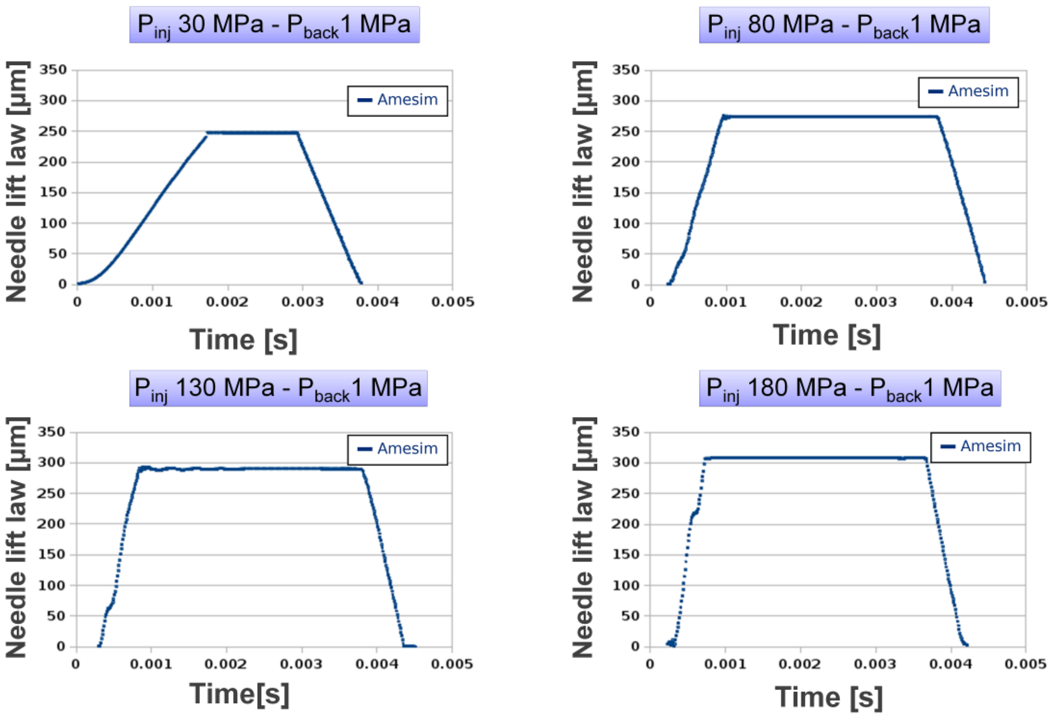

Fig. 12. Needle lift laws used for the transient internal flow simulations

The 1D injector model includes all the geometrical, mechanical and hydraulic information of the internal elements of the injector, extracted from a throughout characterization of each of them. The details of the model build-up and validation are available in [46]. The corresponding needle lift laws are shown in Figure 12. The different maximum lift achieved for each condition is linked to the higher deformation of the needle and piston as the pressure inside the injector increases.

5.2 Numerical results in transient conditions.

For the dynamic internal flow simulations, the position of the needle lift obtained from the Amesim model (starting at 1 μm lift) has been directly introduced into the 3D-CFD code, so that the simulation starts and finishes when the needle is at its closed position. The rest of the boundary conditions, together with the configuration parameters (turbulence model, cell size, numerical schemes, etc.) are maintained equal to the ones already explained for the fixed lift simulations. Figure 13 shows the results of these simulations for the four different levels of injection pressure used along the study (30, 80, 130 and 180 MPa) with a backpressure of 1 MPa.

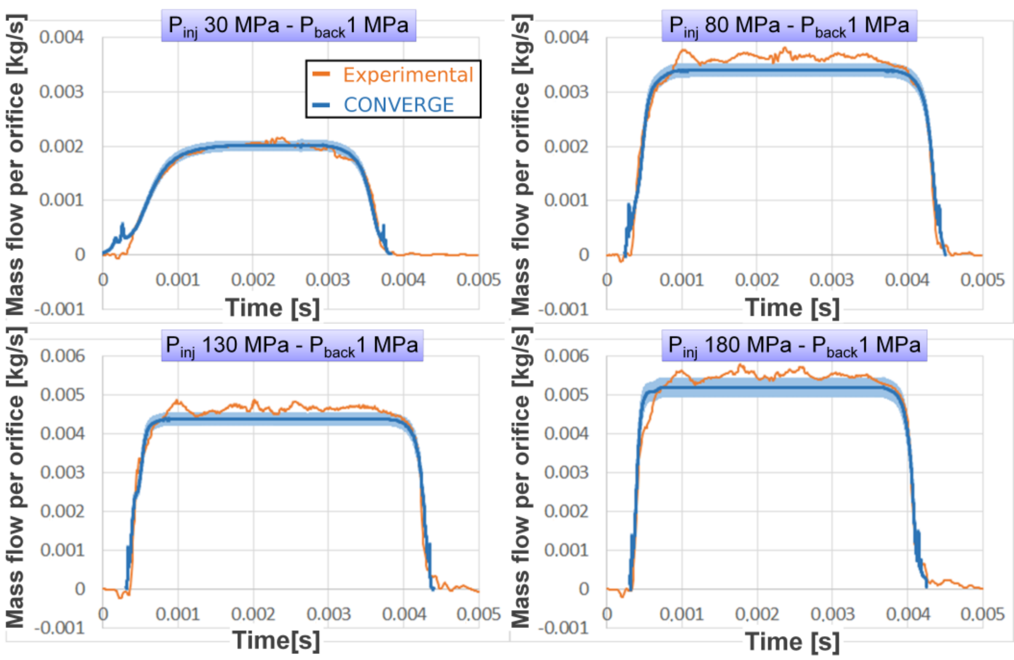

Fig. 13. Mass flow rate profiles: experiments vs modelling.

In this graph, the continuous line represents computed injection rate for the nominal geometry (same as previously used for the steady-state analysis). The shaded area shows the sensitivity of the results to the main nozzle geometry parameters. In this sense, the upper boundary of the shaded area corresponds to a geometry where the inlet rounding radii and the outlet diameter are equal to the average values plus the standard deviation obtained from the silicone molds methodology, and reported on Table 1. This results in values of R_a=37 μm and D_o=126.2 μm. On the contrary, the bottom boundary of the shaded area is obtained with geometrical parameters equal to the average values minus the standard deviation (*i.e*, R_a=21 μm and D_o=121.8 μm). In the steady state region, this results in a sensitivity of approximately ±5% with respect to the nominal geometry in terms of mass flow rate.

As it can be observed, there is a good overall agreement between the numerical and experimental injection rate results for all the cases studied. This is especially clear for the opening and closing phases of the injection event, where the nozzle mass flow is mostly controlled by the needle position, since the most of the pressure drop along the nozzle is found in the needle seat region. Nevertheless, two regions of interest can be identified in the simulation:

- At very low needle lift conditions (start and end of the injection event), a small bump is observed in the mass flow results, especially at low injection pressure. This is related to positions at which only one or two layers of cells with the minimum cell size (approximately 3.2 μm) appear in the needle seat region. This low cell resolution together with the high pressure and velocity gradients appearing in the flow in this area are the source of numerical instabilities, which produce the effect previously described. The fact that this effect is more visible at 30 MPa is related to the slower needle dynamics at this injection pressure, which results in a longer time to achieve the needle lift necessary to overcome this phenomenon. According to a previous work by Battistoni et al. [31], the mass flow at very low needle lifts, and especially during the opening phase of the injection, is also affected by the fact that the fluid domain in the sac is initialized with pressurized liquid fuel. In fact, they noticed that when initializing the sac volume with a pressurized gas, as it would be realistic for a spray simulation, the instabilities almost disappeared. Nevertheless, for the current study a pressurized liquid condition was chosen since it is representative of the conditions during the injection rate measurements. It has to be noted anyway that the magnitude of the mass flow deviation induced by this instability is reduced.

- At steady flow conditions, the simulation considering the nominal geometry does not follow completely the experimental curve. The mass flow in this case is slightly lower than the experimental, which was the trend already observed in the steady-state simulations results (section 4). Closer results are observed when using higher rounding radii and outlet diameter values, although some deviation is still present for mid-to-high injection pressures. Additionally, all the simulations show a flat mass flow in this region, while some oscillations appear in the experimental data. These oscillations are induced by the pressure waves traveling inside the injector during its dynamic behavior, which are not captured in the CFD simulations since a constant pressure boundary condition has been used, and no needle position or inlet pressure fluctuations have been considered.

Finally, the pressure information inside the domain can be seen in Figure 14 as a function on the needle lift. In Figure 14.a, the pressure contours have been plotted in the nozzle middle plane across the orifice for four intermediate needle positions: 35, 67, 94 and 288 µm (maximum needle lift). In this figure, it can be seen that for low needle lifts the pressure drop is mostly located in the needle seat region. This means that the pressure drop across the orifice is reduced, resulting in a low velocity and mass flow condition, as previously seen in figure 13. On the contrary, as the needle moves up the area where the pressure drop is concentrated transitions from the needle seat to the orifice region. Indeed, at maximum needle lift (288 µm) the pressure upstream the orifice is very close to the inlet pressure of the domain. Consequently, the mass flow across the orifice is maximum. When this flow scenario is reached (no significant pressure drop in the needle seat area), the nozzle outlet velocity and consequently the mass flow become independent from the needle position, resulting in the steady-state injection rate area previously analyzed.

This behavior can be seen in further details in Figure 14.b, where the average pressure values along several transversal planes in the needle seat region are detailed. The numbers of the planes are related to the positions highlighted in the 35 µm contour of figure 14.a, being 1 the plane positioned just after the inlet and 10 the plane just before the orifice. Additionally, this information is represented for different needle positions, including the four previously analyzed. According to this figure, the pressure just before the orifice goes as low as 20 MPa for the 35 µm lift, while it is almost equal to the inlet pressure for the last two lifts (221 and 288 µm).

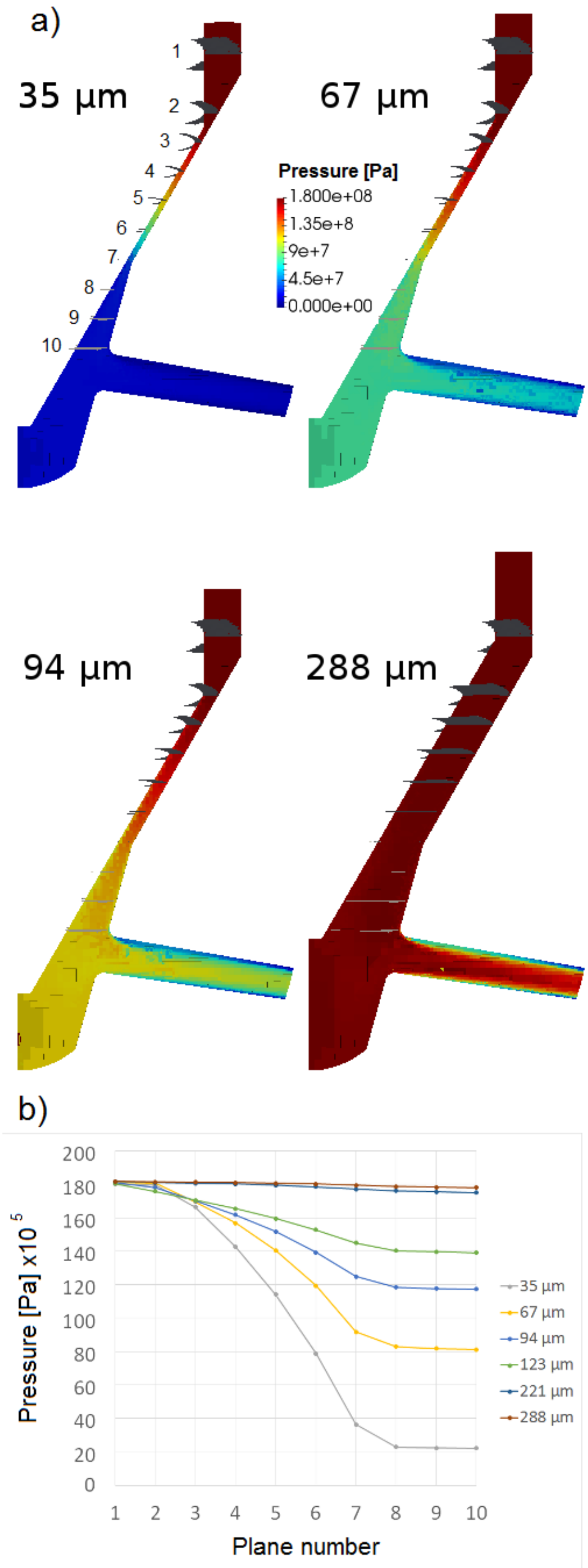

Fig. 14. Pressure data as a function of the needle lift for P_{inj}=180 MPa. a) Contours in the middle plane. b) Average values in different planes across the needle seat region.

6. CONCLUSIONS.

In the current paper, the transient hydraulic performance of a diesel injector during a complete injection event has been evaluated using 3D-CFD simulations. For this purpose, a production solenoid-driven multihole injector has been widely characterized prior to carry out the simulations. In particular, a silicone mold technique has been employed to obtain the geometry of the nozzle sac and orifices, needed to construct the 3D model. Additionally, experiments to determine the injection rate and momentum flux at the nozzle outlet have been done at different boundary conditions, allowing to obtain enough data for a wide validation of the model.

The simulation methodology, including Adaptative Mesh Refinement (AMR) has been first studied and validated on fixed-lift stationary conditions (computed at maximum needle position). A wide parameterization of the numerical schemes for the equations discretization, as well as the cell size parameters, has been performed to find the optimal configuration for the study. Then, some of the main nozzle outlet hydraulic parameters, such as the stationary mass flow rate or the effective velocity, have been computed and compared to the experiments, showing a maximum deviation lower than 10%, which is consistent with previous results without AMR.

Later on, AMR has been used to compute internal nozzle flow at transient needle lift. The needle lift profiles imposed in the 3D-CFD study had been obtained from a previously developed and validated 1D model of the same injector used for the experiments. In these conditions, the methodology used in this study has shown its suitability to compute the flow delivery at very low lifts, which would not be possible with other moving mesh strategies without severe convergence issues. The results show also a good consistency between the experimental and computational injection rates (especially in the opening and closing phases), with maximum deviations similar to the ones obtained at stationary needle lifts. These deviations can be significantly diminished when increasing the orifice inlet rounding radii and outlet diameter within the uncertainty boundaries of the silicone molds methodology. Finally, it is seen that the pressure drop along the domain is strongly related to the needle position, resulting in different velocity and mass flow through the discharge orifices.

ACKNOWLEDGEMENTS.

This work was partly sponsored by "*Ministerio de Economa y Competitividad*", of the Spanish Government, in the frame of the Project "*Estudio de la interacción chorro-pared en condiciones realistas de motor*", Reference *TRA2015-67679-c2-1-R*. The authors would like also to thank the computer resources, technical expertise and assistance provided by Universidad de Valencia in the use of the supercomputer "*Tirant*". Mr. Jaramillo's Thesis is funded by "Conselleria d'Educació, Cultura i Esports" of Generalitat Valenciana in the frame of the program "Programa VALI+D para investigadores en formación, Reference ACIF/2015/040.

References

1. Hall CAS, Lambert JG, Balogh SB (2014) EROI of different fuels and the implications for society. Energy Policy 64:141–152. doi: 10.1016/j.enpol.2013.05.049

2. Lujan JM, Tormos B, Salvador FJ, Gargar K (2009) Comparative analysis of a DI diesel engine fuelled with biodiesel blends during the European MVEG-A cycle: Preliminary study (I). Biomass and Bioenergy 33:941–947. doi: 10.1016/j.biombioe.2009.02.004

3. Pickett LM, Siebers DL (2004) Soot in diesel fuel jets: Effects of ambient temperature, ambient density, and injection pressure. Combust Flame 138:114–135. doi: 10.1016/j.combustflame.2004.04.006

4. Dec JE (1997) A Conceptual Model of DI Diesel Combustion Based on Laser-Sheet Imaging. SAE Tech. Pap. 970873

5. Wang X, Huang Z, Zhang W, et al (2011) Effects of ultra-high injection pressure and micro-hole nozzle on flame structure and soot formation of impinging diesel spray. Appl Energy 88:1620–1628. doi: 10.1016/j.apenergy.2010.11.035

6. Sayin C, Gumus M, Canakci M (2013) Influence of injector hole number on the performance and emissions of a di diesel engine fueled with biodiesel-diesel fuel blends. Appl Therm Eng 61:121–128. doi: 10.1016/j.applthermaleng.2013.07.038

7. Mohan B, Yang W, Chou SK (2013) Fuel injection strategies for performance improvement and emissions reduction in compression ignition engines—A review. Renew Sustain Energy Rev 28:664–676. doi: 10.1016/j.rser.2013.08.051

8. Payri R, Salvador FJ, Gimeno J, De la Morena J (2011) Influence of injector technology on injection and combustion development, Part 1: Hydraulic characterization. Appl Energy 88:1068–1074. doi: http://dx.doi.org/10.1016/j.apenergy.2010.10.012

9. Park SW, Kim JW, Lee CS (2006) Effect of Injector Type on Fuel-Air Mixture Formation of High-Speed Diesel Sprays. Proc Inst Mech Eng Part D J Automob Eng 220:647–659. doi: 10.1243/09544070D20304

10. Moon S, Komada K, Sato K, et al (2015) Ultrafast X-ray study of multi-hole GDI injector sprays: Effects of nozzle hole length and number on initial spray formation. Exp Therm Fluid Sci 68:68–81. doi: 10.1016/j.expthermflusci.2015.03.027

11. Powell CF, Kastengren AL, Liu Z, Fezzaa K (2010) The Effects of Diesel Injector Needle Motion on Spray Structure. J Eng Gas Turbines Power 133:12802. doi: 10.1115/1.4001073

12. Huang W, Moon S, Ohsawa K (2016) Near-nozzle dynamics of diesel spray under varied needle lifts and its prediction using analytical model. Fuel 180:292–300. doi: 10.1016/j.fuel.2016.04.042

13. Sun Z-Y, Li G-X, Chen C, et al (2015) Numerical investigation on effects of nozzle’s geometric parameters on the flow and the cavitation characteristics within injector’s nozzle for a high-pressure common-rail DI diesel engine. Energy Convers Manag 89:843–861. doi: 10.1016/j.enconman.2014.10.047

14. Devassy BM, Habchi C, Daniel E (2015) Atomization Modelling of Liquid Jets

using a Two-Surface Density Approach. At Sprays 25:47–80.

15. Moon S, Gao Y, Park S, et al (2015) Effect of the number and position of nozzle holes on in- and near-nozzle dynamic characteristics of diesel injection. Fuel 150:112–122. doi: 10.1016/j.fuel.2015.01.097

16. Payri R, Salvador FJ, Carreres M, De la Morena J (2016) Fuel temperature influence on the performance of a last generation common-rail diesel ballistic injector. Part II: 1D model development, validation and analysis. Energy Convers Manag 114:376–391. doi: 10.1016/j.enconman.2016.02.043

17. Plamondon E, Seers P (2014) Development of a simplified dynamic model for a piezoelectric injector using multiple injection strategies with biodiesel/diesel-fuel blends. Appl Energy 131:411–424. doi: 10.1016/j.apenergy.2014.06.039

18. Postrioti L, Malaguti S, Bosi M, et al (2014) Experimental and numerical characterization of a direct solenoid actuation injector for Diesel engine applications. Fuel 118:316–328. doi: 10.1016/j.fuel.2013.11.001

19. Desantes JM, Salvador FJ, Lopez JJ, De la Morena J (2011) Study of mass and momentum transfer in diesel sprays based on X-ray mass distribution measurements and on a theoretical derivation. Exp Fluids 50:233–246. doi: 10.1007/s00348-010-0919-8

20. De la Morena J, Neroorkar K, Plazas AH, et al (2013) Numerical analysis of the influence of diesel nozzle design on internal flow characteristics for 2-valve diesel engine application. At Sprays 23:97–118. doi: 10.1615/AtomizSpr.2013006361

21. Duke DJ, Schmidt DP, Neroorkar K, et al (2013) High-resolution large eddy simulations of cavitating gasoline-ethanol blends. Int J Engine Res 14:578–589. doi: 10.1177/1468087413501824

22. Mitroglou N, McLorn M, Gavaises M, et al (2014) Instantaneous and ensemble average cavitation structures in Diesel micro-channel flow orifices. Fuel 116:736–742. doi: 10.1016/j.fuel.2013.08.060

23. Wang X, Li K, Su W (2012) Experimental and numerical investigations on internal flow characteristics of diesel nozzle under real fuel injection conditions. Exp Therm Fluid Sci 42:204–211. doi: http://dx.doi.org/10.1016/j.expthermflusci.2012.04.022

24. Sou A, Pratama RH (2016) Effects of Asymmetric Inflow on Cavitation in Fuel Injector and Discharged Liquid Jet. At Sprays 26:939–959. doi: 10.1615/AtomizSpr.2015013501

25. Xue Q, Battistoni M, Powell CF, et al (2015) An Eulerian CFD model and X-ray radiography for coupled nozzle flow and spray in internal combustion engines. Int J Multiph Flow 70:77–88. doi: 10.1016/j.ijmultiphaseflow.2014.11.012

26. Castilla R, Gamez-Montero PJ, Ertrk N, et al (2010) Numerical simulation of turbulent flow in the suction chamber of a gearpump using deforming mesh and mesh replacement. Int J Mech Sci 52:1334–1342. doi: 10.1016/j.ijmecsci.2010.06.009

27. Parlak Z, Engin T (2012) Time-dependent CFD and quasi-static analysis of magnetorheological fluid dampers with experimental validation. Int J Mech Sci

64:22–31. doi: 10.1016/j.ijmecsci.2012.08.006

28. Chiatti G, Chiavola O, Palmieri F (2009) Spray Modeling for Diesel Engine Performance Analysis. SAE Tech Pap 2009-01-0835. doi: 10.4271/2009-01-0835

29. Marcer R, Audiffren C, Viel A, et al (2010) Coupling 1D System AMESim and 3D CFD EOLE models for Diesel Injection Simulation Renault. In: ILASS - Eur. 2010, 23rd Annu. Conf. Liq. At. Spray Syst. pp 1–10

30. Desantes JM, Salvador FJ, Carreres M, Martínez-López J (2014) Large-eddy simulation analysis of the influence of the needle lift on the cavitation in diesel injector nozzles. Proc Inst Mech Eng Part D J Automob Eng 229:407–423. doi: 10.1177/0954407014542627

31. Battistoni M, Xue Q, Som S (2016) Large-Eddy Simulation (LES) of Spray Transients : Start and End of Injection Phenomena. Oil Gas Sci Technol - Rev d’IFP Energies Nouv 71:24. doi: http://dx.doi.org/10.2516/ogst/2015024

32. CONVERGE is a trade mark of Convergent Science https://convergecfd.com.

33. Macian V, Bermúdez V, Payri R, Gimeno J (2003) New technique for determination of internal geometry of a Diesel nozzle with the use of silicone methodology. Exp Tech 27:39–43. doi: 10.1111/j.1747-1567.2003.tb00107.x

34. Dabiri S, Sirignano W a., Joseph DD (2007) Cavitation in an orifice flow. Phys Fluids 19:72112. doi: 10.1063/1.2750655

35. Mohan B, Yang W, Chou SK (2014) Cavitation in Injector Nozzle Holes - A Parametric Study. Eng Appl Comput Fluid Mech 8:70–81.

36. Salvador FJ, Hoyas S, Novella R, Martinez-Lopez J (2011) Numerical simulation and extended validation of two-phase compressible flow in diesel injector nozzles. Proc Inst Mech Eng Part D J Automob Eng 225:545–563. doi: 10.1177/09544070JAUTO1569

37. Som S, Longman DE, Ramirez AI, Aggarwal S (2012) Influence of Nozzle Orifice Geometry and Fuel Properties on Flow and Cavitation Characteristics of a Diesel Injector. In: Fuel Inject. Automot. Eng. pp 112–126

38. Desantes JM, Salvador FJ, Carreres M, Jaramillo D (2015) Experimental Characterization of the Thermodynamic Properties of Diesel Fuels Over a Wide Range of Pressures and Temperatures. SAE Int J Fuels Lubr 8:2015-01–0951. doi: 10.4271/2015-01-0951

39. Bosch W (1966) The Fuel Rate Indicator: a New Measuring Instrument for Display of the Characteristics of Individual Injection. SAE Pap. 660749

40. Payri R, Salvador FJ, Gimeno J, Bracho G (2008) A new methodology for correcting the signal cumulative phenomenon on injection rate measurements. Exp Tech 32:46–49. doi: 10.1111/j.1747-1567.2007.00188.x

41. Payri F, Payri R, Salvador FJ, Martínez-López J (2011) A contribution to the understanding of cavitation effects in Diesel injector nozzles through a combined experimental and computational investigation. Comput Fluids 58:88–101. doi: 10.1016/j.compfluid.2012.01.005

42. Lichtarowicz AK, Duggins RK, Markland E (1965) Discharge coefficients for incompressible non-cavitating flow through long orifices. J Mech Eng Sci 7:210–

219. doi: 10.1243/JMES_JOUR_1965_007_029_02

43. Lopez JJ, Salvador FJ, De la Garza OA, Arrègle J (2012) Characterization of the pressure losses in a common rail diesel injector. Proc Inst Mech Eng Part D-Journal Automob Eng 226:1697–1706. doi: 10.1177/0954407012447020

44. Salvador FJ, Carreres M, Jaramillo D, Martínez-López J (2015) Comparison of microsac and VCO diesel injector nozzles in terms of internal nozzle flow characteristics. Energy Convers Manag 103:284–299. doi: 10.1016/j.enconman.2015.05.062

45. LMS (2010) Imagine.Lab AMESim v.10. User's manual.

46. Payri R, Salvador FJ, Martí-Aldaraví P, Martínez-López J (2012) Using one-dimensional modeling to analyze the influence of the use of biodiesels on the dynamic behavior of solenoid-operated injectors in common rail systems: Detailed injection system model. Energy Convers Manag 54:90–99. doi: 10.1016/j.enconman.2011.10.007